

Pressure stimulus study on acupuncture points with multi-channel multimode-fiber diffuse speckle contrast analysis (MMF-DSCA)

JAE YOON PARK, GISOON CHOI, AND KIJOON LEE* 

Department of Electrical Engineering and Computer Science, Daegu Gyeongbuk Institute of Science and Technology (DGIST), Daegu, Republic of Korea

*kjlee@dgist.ac.kr

Abstract: A multi-channel multimode-fiber deep tissue flowmetry system has been constructed based on diffuse speckle contrast analysis (DSCA) for simultaneous blood flow measurements at different locations on the human body. This system has been utilized in an acupuncture study within the field of traditional Chinese medicine (TCM), primarily focusing on acupuncture points along the large intestine meridian. Deep tissue blood flow was monitored at four different acupuncture points (LI1, LI5, LI10, and ST25) with a sampling rate of 60 Hz while applying pressure stimulus on LI4 (hegu or hapgok). Although the blood flow index (BFI) and blood volume (BV) did not exhibit significant changes after the pressure stimulus, an increase in the amplitude and complexity of low-frequency oscillations (LFOs) in microcirculation was observed.

© 2023 Optica Publishing Group under the terms of the [Optica Open Access Publishing Agreement](#)

1. Introduction

As traditional Chinese medicine (TCM) gains recognition as an alternative and holistic approach for human health, acupuncture studies are also attracting increasing attention [1]. Although the mechanism by which acupuncture practices bring about therapeutic effects is not well-studied, it is believed that acupuncture affects autonomic nervous system, thereby regulating microcirculations. The literature reports various alterations of microcirculation as a result of acupuncture [2].

In this paper, we report on the modulation of microcirculation following a series of pressure stimulus on acupuncture points (acupoints). We monitored deep tissue microcirculation, rather than superficial microcirculation, by using a multimode fiber-based diffuse speckle contrast analysis (MMF-DSCA) system with a source-detector distance of approximately 1 cm. This ensures that our detected blood flow index (BFI) primarily originates from a deep tissue region at a depth of approximately 0.5 cm [30,31]. This differentiates our study from other acupuncture-related studies which employ superficial flow measurement techniques such as laser Doppler perfusion imaging (LDPI) or transcutaneous oxygen pressure (TcPO₂).

When analyzing the detected BFI signal, we specifically focus on the behavior of low frequency oscillation (LFO) with a period longer than 10s. The LFOs is known to be related to vascular health [3], and we will discuss its changes in both amplitude and complexity.

1.1. Acupoints in TCM

According to TCM theory, a human body has 12 meridians which are considered pathways for the flow of Qi. Each meridian is named after a specific internal organ that the meridian is known to be related with. Along these meridians, numerous acupoints exist. Acupoints not only serve as treatment points where acupuncture needle or moxibustion can be applied, but also act as diagnostic points.

Among the 12 meridians, Large Intestine meridian (LI) begins at the tip of the index finger and extends along the arm and shoulder. Within the LI meridian, LI4 (hegu, hapgok) is widely

recognized as a popular point for stimulating analgesic effect [4–6]. In our study, LI4 was chosen as a stimulation point, while LI1, LI5, LI10, ST25 were selected as diagnostic points. ST25 (Tianshu or Cheonchu) is the mu point of the LI meridian, primarily used for treating the corresponding organ (the large intestine, in this case).

A low-frequency oscillation (LFO) with a period longer than 10s, also known as vasomotor wave or Mayer wave, is known to be present when monitoring local hemodynamic variable [3,7,32,33]. This oscillation is believed to originate from sphincters located between arterioles and capillaries, regulating the amount of microcirculation in local tissue. As the amplitude and complexity of LFO have been reported to be related to the health of blood vessels [8], we will mainly analyze the LFOs observed from our microcirculation measurement to determine if there are any changes in amplitude and/or complexity following the pressure stimulus

1.2. Diffuse speckle contrast analysis

Diffuse Correlation Spectroscopy (DCS) offers a scientifically rigorous approach to investigate deep tissue blood flow. It is based on the solution of the correlation diffusion equation, which resembles photon diffusion equation that is commonly employed in diffuse optics. While DCS is considered the most standard method for non-invasive deep tissue flow monitoring, it does have drawbacks including high instrumentation cost, high computational load, and a low sampling rate. This is due to the requirement of generating a quality auto-correlation curve and fitting it to a model function.

To address the limitations of DCS, Diffuse Speckle Contrast Analysis (DSCA) [9,10] was developed in 2013. This technique leverages the fact that the speckle contrast of an image, obtained with a finite exposure time, contains information on the dynamics of scatterers along the light paths. The underlying principle is similar to that of laser speckle contrast imaging (LSCI), a well-known method used for imaging blood vessels in the superficial layer [11]. However, DSCA extends this approach to deep tissue probing by separating the source and detector optodes by centimeters.

Theoretically, DSCA can be understood in relation to DCS as follows. The speckle contrast K , which is defined as the ratio between the standard deviation and the mean intensity (i.e., $K = \sigma/I$), is related to field autocorrelation function $g_1(\tau)$ through the following equation [12]

$$K^2 = \frac{2\beta}{T} \int_0^T \left(1 - \frac{\tau}{T}\right) |g_1(\tau)|^2 d\tau$$

where T represents the exposure time and β is a constant associated with the collecting optics. From the above equation, it is evident that the speckle contrast is essentially a weighted integral of $g_2(\tau) - 1$, with a higher weightage on smaller delay times, where $g_2(\tau)$ is an intensity autocorrelation function that can be obtained from DCS. Therefore, the value of K reflects the rate of decay of the autocorrelation curve. In DSCA, the reciprocal of K^2 is used as a blood flow index (BFI), and its relationship with blood flow is known to exhibit a close-to-linear behavior within the physiologically relevant flow range [13].

The recent advancements in DSCA has allowed us to achieve even higher frame rates by utilizing multimode fiber (MMF) as the detector fiber [14]. Since the statistical properties of speckle structure are largely preserved during short propagation through an MMF, the need for using single-mode fiber (SMF) on the detector side has been eliminated in most practical scenarios. This breakthrough has opened up the possibility of spatial DSCA with concurrent multi-channel operation. This concept has been recently applied to measure pulse wave velocity on the human arm, providing a convenient means to monitor changes in blood pressure [15].

In this paper, we present a multi-channel MMF-DSCA device capable of simultaneously monitoring blood flow index (BFI) from up to 7 different positions on the human body. With the aim of applying this instrument in TCM-related studies, we conducted a preliminary study

to monitor BFIs on four acupoints of healthy subjects during a pressure stimulus. The data from this four-channels were analyzed using various approaches, including time-domain analysis, frequency-domain analysis, and complexity analysis.

2. Methods

Our main tool for deep tissue blood flowmetry is a multi-channel multimode-fiber DSCA (MMF-DSCA) device. The details of the multi-channel MMF-DSCA system and the experimental protocol are described below.

2.1. Multi-channel multimode-fiber DSCA system and optical probes

A fiber-coupled 100 mW 808 nm single longitudinal mode (SLM) laser with a long coherence length (CrystaLaser) was used as the light source. The total power was split into four source fibers using consecutive fiber beam splitters. On the detector side, a 1×7 fan-out fiber bundle with 200-micron core MMF (Thorlabs, BF72HS01) was employed to couple the detected light onto a CCD camera (Basler, acA1300-60gm) using a lens system of unit magnification. Four custom-made probes were utilized, each consisting of a source fiber with an FC bare ferrule and a detector fiber with an SMA bare ferrule, secured in position with 1 cm distance between them. One of the probes, designed to be placed on a finger, was configured in transmission mode due to its geometric constraints, as shown in Fig. 1.

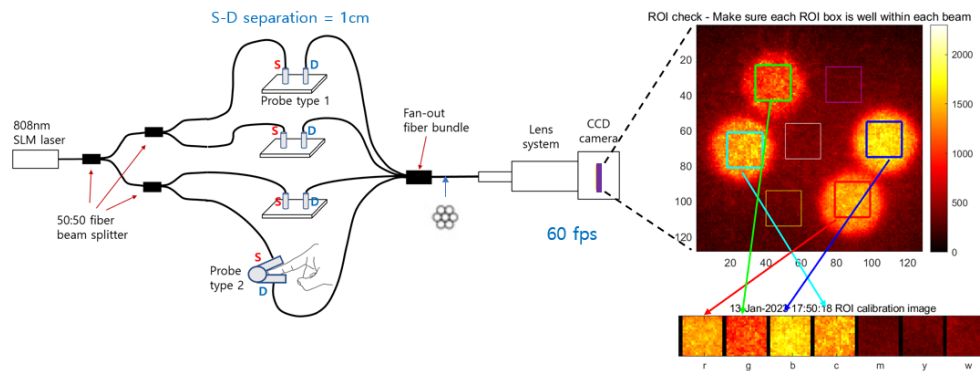


Fig. 1. Schematic of multi-channel MMF-DSCA system for 4-channel acupoint study.

Four of the seven detector channels are being used, where each detector collects diffusely transmitted light from four different locations on the subject. A typical CCD image within an ROI of 128×128 pixels is shown on the right, where the center positions of each channel were identified, and a 21×21 square region (appearing as seven different colored boxes) around each center was used for data sampling. Each channel was color-coded in the sequence of 'rgbcmyw' starting with red and ending with white, and only 'rgbc' channels were used for acupoint study.

A custom-made program coded in MatLab (Natick, MA) was used to operate the camera, which enables users to check for the raw speckle patterns on each channel in the preparation stage, and displays the trends of BFI in realtime during actual data acquisition. For the pressure stimulus study, four of the seven channels (red, green, blue, and cyan) were utilized.

The MMF-DSCA system was operated at 60 frames per second with a 2 ms exposure time. Prior to initiating the actual data acquisition, the CCD image was monitored in live-mode to ensure that the image was not saturated.

2.2. Validation study

A validation study was conducted using an arm-cuff protocol to determine whether the multi-channel MMF-DSCA device exhibited the expected results of physiological blood flow. Two index fingers of a subject were selected for blood flow monitoring, while a pressure cuff was applied to one arm with a pressure of 220mmHg to induce arterial occlusion for 2 minutes (Fig. 2). Additionally, one channel was connected to a static optical phantom that mimicked human tissue to assess the level of speckle fluctuation caused by the light source itself. The static optical phantom has been made with PDMS, titanium dioxide, and india ink, following recipes in the literature [34], and its optical properties are measured to be $\mu_a \sim 0.006 \text{ mm}^{-1}$ and $\mu'_s \sim 1 \text{ mm}^{-1}$ at 650 nm.

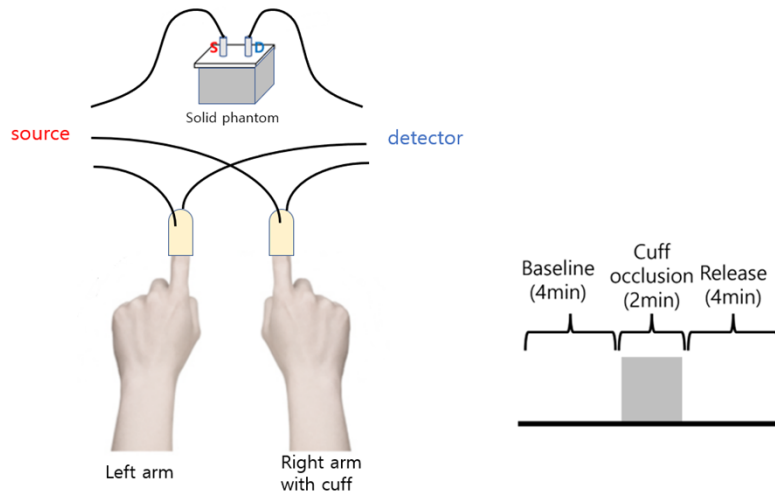


Fig. 2. Schematic and protocol for validation study BFIs from two LI1 positions from each hand were monitored while another channel was connected to a stationary solid phantom to see the effects of source fluctuations on BFI measurement (left). The timing protocol for the validation study is shown, where 2-min cuff occlusion was performed on the right arm only (right)

2.3. Pressure stimulus study protocol

Four blood flow probes were utilized on four different acupoints as shown in Fig. 3: LI1, LI5, LI10, and ST25. Three acupoints (LI1, LI5, LI10) were selected on the lower arm along the LI meridian, and ST25 on the abdomen was selected as it is the mu point of LI meridian. The probes were securely positioned on the body using straps, except the one on fingertip (LI1) which operated in transmission mode by using a clip-like contraption. The straps were fastened just enough so that fiber tips make a good contact with tissue, while it does not cause too much pain for subjects. Care was taken so that the pressure applied on the tissue is constant, in order to prevent any pressure-induced hemodynamic changes reported in literature [35–37].

Four healthy male subjects in their 20s were recruited for this study. The subjects were instructed to lie down on a bed in supine position during the measurements. After checking the CCD image for proper alignment and exposure, the experimental protocol started, consisting of a 5-minute baseline period, followed by 2-minute 20-second pressure application period, and finally another 5-minute release period. The pressure application period involved four separate events of applying pressure for 20 seconds, with 20 seconds of rest periods in between each pressure application. A spring-loaded pressure rod has been used, where a force of 10 N has

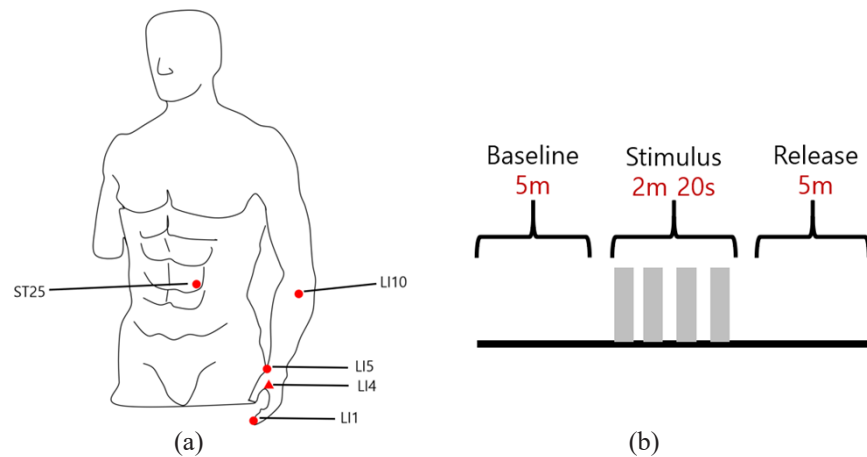


Fig. 3. Acupoints and protocol for pressure stimulus experiment (a) Acupoints used for pressure application (triangle) and for blood flow monitoring (circle). (b) Timing diagram of pressure stimulus protocol, where grey bars indicate the time period where pressure is applied.

been consistently applied on LI4 acupoint. It was made possible by pre-marking the compressed length of the pressure rod for a force of 10 N.

3. Results

3.1. Validation study

The results from the cuff-occlusion protocol from one subject are presented in Fig. 4, with a moving average filter being applied. Since the arm cuff was only applied to the right arm, the decrease in blood flow index (BFI) during cuff occlusion is observed only in the right index finger. The BFI level of the right index finger drops to less than 20% of the baseline value, which aligns with physiological expectations. The 3rd channel, which was placed on a static optical phantom, exhibits mild fluctuation around a very low BFI value (~25) compared to the finger measurements (>120). This suggests that the fluctuations originating from the light source itself does not contribute significantly to BFI signal *in-vivo*. For more details including arguments on noise issue, see [Supplement 1](#).

In addition to the BFI measurement, the CCD images obtained from the MMF-DSCA can be summed over each region of interest (ROI) to generate a photoplethysmography (PPG) signal. More precisely, by taking minus logarithm of the summed intensity, one can obtain a quantity that is proportional to blood volume (BV). This BV signal can be plotted alongside the BFI signal as shown in Fig. 5, enabling simultaneous observation of the two hemodynamic signals. The cuff-occlusion experiment was performed on four healthy subjects in total, and they all showed similar behavior as shown in Fig. 5.

As depicted in Fig. 5, both the BFI and BV signals show a clear heartbeat pattern, with the BFI signal tending to lead the BV signal. A magnified version of above graph is shown in Fig. S3 in [Supplement 1](#) for better visualization of this behavior, which is consistent with what has been reported in recent literature [25–27]. Furthermore, during arterial occlusion, it is observed that the BFI decays much more rapidly than the BV does, as shown in the yellow-shaded region in the second graph in Fig. 5.

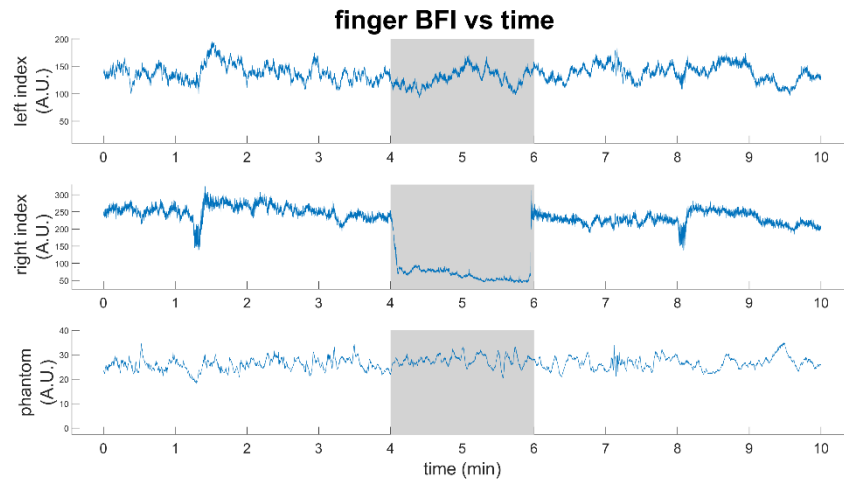


Fig. 4. BFI data from single-sided arm-cuff protocol for validation study. Grey region represents the cuff-occlusion period where arterial occlusion is induced on the right arm only. As expected, a sudden drop of BFI by more than 80% is observed from the right index finger channel, while left index finger channel shows no sign of BFI decrease.

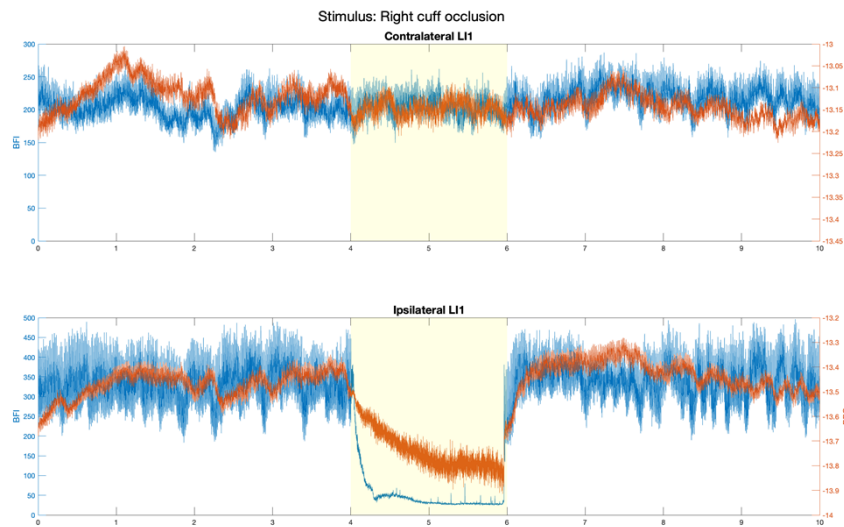


Fig. 5. Blood flow (blue, BFI) and blood volume (orange, BV) data from index fingers of both hands during cuff occlusion on the right arm. Cuff occlusion period is represented as pale yellow area. Heartbeat signal is much better observed from BFI than from BV signal (See Fig. S3 in [Supplement 1](#) for magnified graph). Also, response to arm cuff inflation is much faster in BFI than in BV, as shown in the ipsilateral LI1 graph.

3.2. Pressure stimulus study

The application of pressure on LI4 results in changes in BFI, as illustrated in Fig. 6. The graph displays a dataset from one subject as an example, where all four channels exhibit distinct baseline values and different behaviors. (A set of comprehensive graphs showing all four subjects' data are shown in Fig. S1 in [Supplement 1](#), where the behavior of BV is also plotted.)

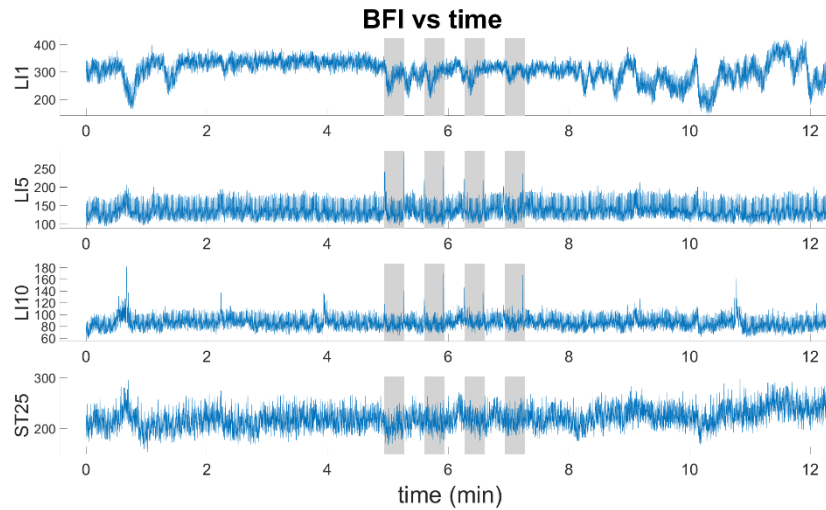


Fig. 6. Measured blood flow index (BFI) during pressure stimulus protocol. Grey shaded area denotes the application of pressure. A moving average filter with window size of 10 was applied.

One common observation among the subjects was the presence of motion artifacts in the LI5 and LI10 channels, caused by the motion of the pressure rod. This occurrence is unavoidable since LI5 and LI10 are in close proximity to LI4 position where the pressure is directly applied. A distinct sharp peak can be observed at the onset and offset of pressure application. On the other hand, BFI from LI1 consistently shows a drop at the onset of each pressure application. This is due to LI1 being in the distal part relative to LI4, and the pressure on LI4 tends to impede the blood flow in LI1. However, the BFI quickly recovers after each drop, and the average value does not differ significantly from the baseline value.

While the BFI graph does show some effect of pressure stimulus, the overall behavior of BFI after the stimulus is not significantly different from the baseline. As depicted in Fig. 7, the BFI at release does not exhibit any statistically significant difference compared to the baseline. It is worth noting that the average BFI values across all four channels are distinct from one another, and they also vary among the subjects. (A set of plots with all subjects' data are shown in Fig. S2 in [Supplement 1](#)) This suggests that the level of microcirculation is highly dependent on the individual and the specific location being measured. Therefore, it is more meaningful to measure the relative BFI compared to a baseline value in general.

3.3. Low frequency oscillation study

A scalogram was created by using wavelet toolbox in MatLab for each BFI data, providing a time-frequency analysis as shown in Fig. 8. Several features can be observed from the scalogram.

First, the pressure application event is clearly visible in channels LI5 and LI10, as the motion artifact resembles delta-function that has almost all frequency components and produces a distinct vertical feature on the scalogram. This observation is consistent with the raw BFI data shown in Fig. 6.

Secondly, the heartbeat frequency and its harmonics are clearly seen in all four channels. The fundamental frequency is observed at approximately 1 Hz, and its harmonic structure varies across channels, indicating different pulse shapes in different locations.

Thirdly, the low frequency oscillation (LFO) in the 0.05~0.15 Hz range appears to have increased after the pressure stimulus, particularly in LI1. This observation deserves some

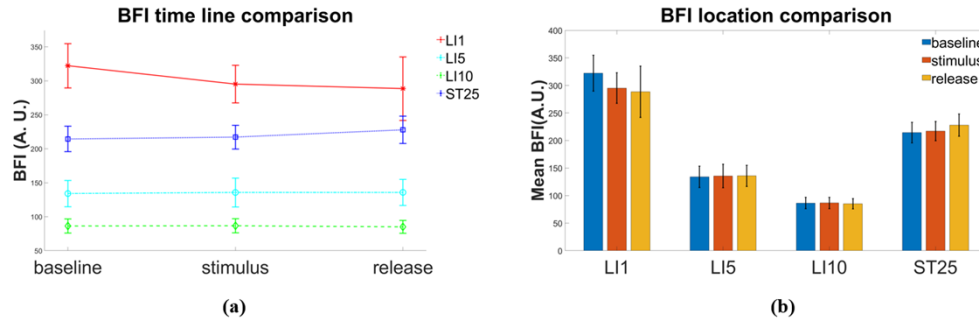


Fig. 7. Overall BFI change of four different channels during pressure stimulus protocol for one subject (S1). Baseline BFIs differ much depending on channel positions, but mostly maintains its value throughout the stimulus and release period (a). Another visualization using a bar-graph is shown, where not much change in BFI is observed per location (b).

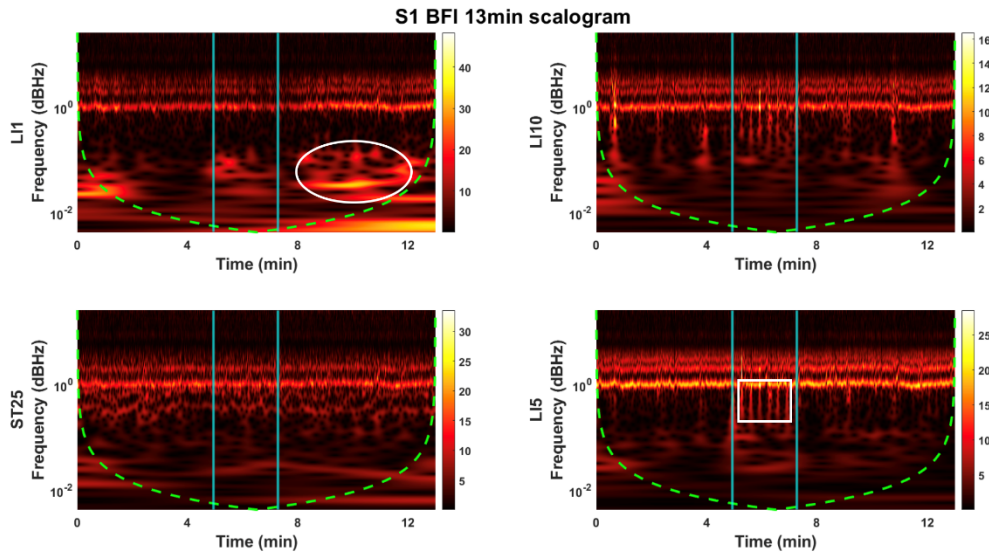


Fig. 8. Scalogram of 4-ch BFI data from S1. Frequency axis is in logarithmic scale, and the onset and offset of pressure stimulus is denoted as two vertical cyan lines. The cone of influence is denoted as green dashed curve, which delineates the region where edge artifact prevails. The region denoted by white oval is where increase of LFOs is prominent, and the region in white rectangle shows motion artifacts due to onset and offset of pressure application, which is most prominent on LI5 due to its proximity to stimulus point (LI4).

attention, considering the emphasis placed on LFOs in vascular health. (The LFO in this frequency range has been studied along with microscopic imaging [28], and its myogenic origin has been found [29])

As we observed changes in LFO using the scalogram, we proceeded to obtain the low-pass filtered signal of the LFO and conducted complexity analysis. We used the *designfilt* function in MatLab to design a low-pass FIR filter, with passband frequency of 0.15 Hz, stopband frequency of 0.2 Hz, passband ripple of 0.2 Hz, stopband attenuation of 65 dB, and Kaiser window. Figure 9(a) presents the low-pass filtered signal for all four channels. Specifically, on

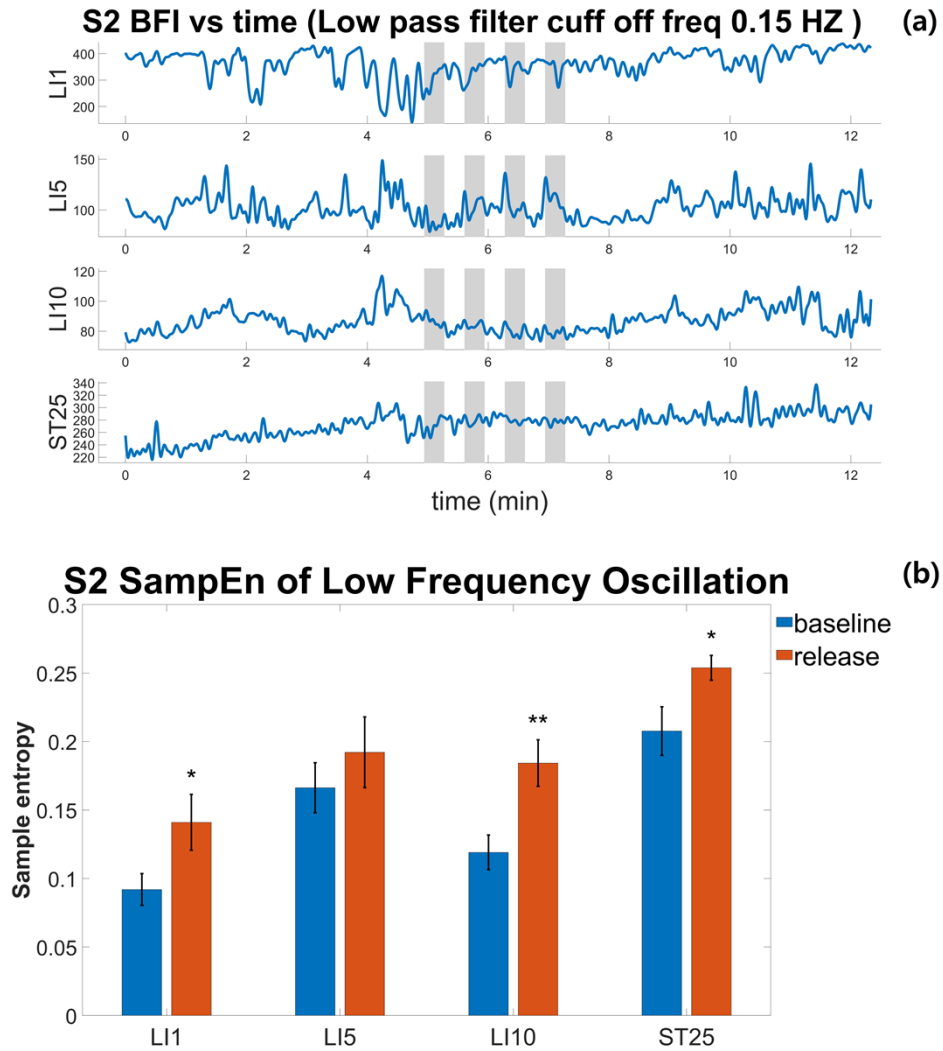


Fig. 9. Low-pass filtered data which shows low frequency oscillation (a) and its SampEn values (b) for S2. Asterisk on the graph indicates $p < 0.05$, while the double asterisk represents $p < 0.01$. The error bars represent standard errors.

LI1, noticeable alterations after the pressure stimulus can be observed in both the oscillating amplitude and its pattern.

On the low-pass filtered signal, we applied sample entropy (SampEn) analysis which is one of the complexity analysis methods that is gaining popularity especially in biomedical signal analysis [16]. It is an improved version of its predecessor, approximate entropy (ApEn) and offers better properties in many aspects [17]. In a nutshell, SampEn gives a measure of how *unlikely* it is for a pattern (a template vector) to be repeated when the template size is increased by one. The definition is presented below, with the template size of 2 which is the case used in this paper

$$\text{SampEn} = -\ln \frac{[\# \text{ of 3 dimensional template pairs with distance} < r]}{[\# \text{ of 2 dimensional template pairs with distance} < r]}$$

where a proper distance function has to be used and a small constant r has to be determined. We have used Chebyshev distance as a distance function and $r = 0.2\sigma$ for our data analysis, where σ is the overall standard deviation of the timeseries data.

The purpose of the sample entropy analysis is to find out if there are any changes in complexity in the low frequency oscillation. The Fig. 9(a) showcases a low-pass filtered BFI data of the subject 2.

The low-pass filtered BFI data in Fig. 9(a) for subject 2 was pre-processed for SampEn calculation as follows. A dataset with the duration of 90s was retrieved with the sampling rate of 6 Hz (10-to-1 down-sampling) from both baseline and release period, and the next dataset is retrieved the same way with the starting time point translated by 30s. By continuing to do so, 8 different datasets are prepared from both baseline and release period. One SampEn is calculated from each dataset so that each group has 8 SampEn's, and the Student t -test [38] was performed between the two groups. Table 1 lists the complete results obtained.

Table 1. Two-sample t-test results of sample entropy values between baseline and release

	S1			S2			S3			S4		
	mean \pm std		P value	mean \pm std		P value	mean \pm std		P value	mean \pm std		P value
	baseline	release		baseline	release		baseline	release		baseline	release	
LI1	0.13 \pm 0.07	0.15 \pm 0.03	0.29	0.09 \pm 0.03	0.14 \pm 0.06	0.03	0.07 \pm 0.003	0.06 \pm 0.04	0.64	0.17 \pm 0.05	0.14 \pm 0.04	0.92
LI5	0.22 \pm 0.08	0.24 \pm 0.04	0.22	0.17 \pm 0.05	0.19 \pm 0.07	0.21	0.11 \pm 0.01	0.35 \pm 0.06	2.1×10^{-8}	0.09 \pm 0.02	0.13 \pm 0.04	0.02
LI10	0.15 \pm 0.05	0.19 \pm 0.07	0.08	0.12 \pm 0.04	0.18 \pm 0.05	0.004	0.14 \pm 0.02	0.22 \pm 0.04	2.3×10^{-5}	0.17 \pm 0.02	0.18 \pm 0.02	0.15
ST25	0.19 \pm 0.08	0.16 \pm 0.05	0.84	0.21 \pm 0.05	0.25 \pm 0.03	0.02	0.16 \pm 0.04	0.21 \pm 0.04	0.02	0.18 \pm 0.05	0.23 \pm 0.07	0.04

It should be noted in Table 1 that 3 out of 4 subject shows significant increase in SampEn from ST25, and all 4 subjects showed increased mean of SampEn in LI5 and LI10 positions.

4. Discussion

4.1. Complexity analysis of low frequency oscillation (LFO)

We performed a sample entropy (SampEn) calculation for complexity analysis, out of myriads of complexity measures that can be applied to time-series data, such as fuzzy entropy, distribution entropy, and permutation entropy. Each complexity measure has its own merits and drawbacks, but SampEn is a suitable measure in our case due to its data size-independence, robustness against motion artifacts, and its popularity in biomedical field [18–21].

We observed a significant increase in SampEn value after the pressure stimulation, although the location where SampEn increases vary from subject to subject. This overall trend suggests the pressure stimulation on LI4 may have caused a short-term beneficial effect in terms of vascular health. Although still controversial, low SampEn value of many biomedical time-series signal has been shown to indicate a state with a lesion or a disease [22–24].

4.2. Independent component analysis (ICA)

As we can concurrently monitor the blood flow data from upto 7 channels, it can be demonstrated that a multi-channel analysis such as independent component analysis (ICA) can be applied. As is popularly used in 10-20 system EEG signal analysis, one can apply this technique in multi-channel MMF-DSCA in order to identify several independent sources with different patterns.

As shown in Fig. 10, when ICA is performed with the assumption of three independent sources, we can see that a heartbeat signal is identified as the biggest independent component. The other independent components are supposed to be devoid of heart beat, so it opens up a new possibility of microcirculation study without interferences from heart beat which is observed anytime anywhere. The second and third independent components in Fig. 10(b) could be further analyzed

using time-frequency analysis and/or complexity measures, which we hope will represent the dynamics of Large Intestine meridian.

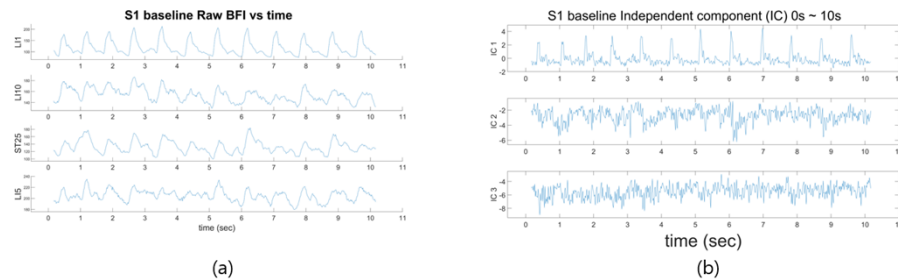


Fig. 10. Example of independent component analysis with four channel BFI data. A sharp heartbeat signal appears as the biggest independent component (IC 1)

5. Conclusion

A multi-channel MMF-DSCA device has been built and validated with arm-cuff protocol, and was successfully applied to a pressure stimulus study whose protocol is meaningful in the context of traditional Chinese medicine. The results show that low-frequency oscillation of the BFI, after a series of pressure stimuli, increases significantly in both its amplitude and complexity. This discovery warrants further investigation through a larger-scale study with various types of stimulus. Future work will involve fully utilizing the 7-channel capability for depth-dependent monitoring of blood flow and incorporating the use of a real acupuncture needle for comprehensive TCM research.

Funding. Daegu Gyeongbuk Institute of Science and Technology (Start-up Fund, 22-BRP-11); National Research Foundation of Korea (2022M3A9B6082790).

Acknowledgments. K. Lee thanks support from DGIST including the start-up fund and Creative Challenge Research Fund (22-BRP-11). A support from National Research Foundation (NRF) of Republic of Korea is also appreciated, for generous funding entitled “Development of ICT-based convergence system for acupuncture treatment based on original technology for acupoints stimulation and diagnosis” (2022M3A9B6082790).

Disclosures. The authors declare no conflicts of interest.

Data availability. Data underlying the results presented in this paper are not publicly available at this time but may be obtained from the authors upon reasonable request.

Supplemental document. See [Supplement 1](#) for supporting content.

References

1. S. Liu, Z. Wang, Y. Su, Q. Lu, W. Yang, M. Fu, X. Jing, Y. Wang, and Q. Ma, “A neuroanatomical basis for electroacupuncture to drive the vagal–adrenal axis,” *Nature* **598**(7882), 641–645 (2021).
2. S. Min, H. Lee, S. Kim, J. Park, Y. Chae, H. Lee, and H. Park, “Local Changes in Microcirculation and the Analgesic Effects of Acupuncture: A Laser Doppler Perfusion Imaging Study,” *J. Altern. Complement. Med.* **21**(1), 46–52 (2015).
3. Y. Tong, L. M. Hocke, S. C. Licata, and B. d. Frederick, “Low-frequency oscillations measured in the periphery with near-infrared spectroscopy are strongly correlated with blood oxygen level-dependent functional magnetic resonance imaging signals,” *J. Biomed. Opt.* **17**(10), 1 (2012).
4. H. Hsiu, W.-C. Hsu, C.-L. Hsu, and S.-M. Huang, “Assessing the effects of acupuncture by comparing needling the hegu acupoint and needling nearby nonacupoints by spectral analysis of microcirculatory laser doppler signals,” *Evid. Based Complement. Alternat. Med.* **2011**, 1–9 (2011).
5. C. J. Zaslowski, D. Cobbin, E. Lidums, and P. Petocz, “The impact of site specificity and needle manipulation on changes to pain pressure threshold following manual acupuncture: a controlled study,” *Complement. Ther. Med.* **11**(1), 11–21 (2003).
6. W. Li, D. Cobbin, and C. Zaslowski, “A comparison of effects on regional pressure pain threshold produced by deep needling of LI4 and LI11, individually and in combination,” *Complement. Ther. Med.* **16**(5), 278–287 (2008).

7. Y. Tong, L. M. Hocke, and B. B. Frederick, "Low Frequency Systemic Hemodynamic "Noise" in Resting State BOLD fMRI: Characteristics, Causes, Implications, Mitigation Strategies, and Applications," *Front. Neurosci.* **13**, 787 (2019).
8. A. Sassaroli, M. Pierro, P. R. Bergethon, and S. Fantini, "Low-Frequency Spontaneous Oscillations of Cerebral Hemodynamics Investigated With Near-Infrared Spectroscopy: A Review," *IEEE J. Sel. Top. Quantum Electron.* **18**(4), 1478–1492 (2012).
9. R. Bi, J. Dong, and K. Lee, "Deep tissue flowmetry based on diffuse speckle contrast analysis," *Opt. Lett.* **38**(9), 1401–1403 (2013).
10. R. Bi, J. Dong, and K. Lee, "Multi-channel deep tissue flowmetry based on temporal diffuse speckle contrast analysis," *Opt. Express* **21**(19), 22854–22861 (2013).
11. A. K. Dunn, H. Bolay, M. A. Moskowitz, and D. A. Boas, "Dynamic Imaging of Cerebral Blood Flow Using Laser Speckle," *J. Cereb. Blood Flow Metab.* **21**(3), 195–201 (2001).
12. R. Bi, J. Dong, C. L. Poh, and K. Lee, "Optical methods for blood perfusion measurement—theoretical comparison among four different modalities," *J. Opt. Soc. Am. A* **32**(5), 860–866 (2015).
13. J. Liu, H. Zhang, Z. Shen, J. Lu, and X. Ni, "Quantitatively assessing flow velocity by the slope of the inverse square of the contrast values versus camera exposure time," *Opt. Express* **22**(16), 19327–19336 (2014).
14. R. Bi, Y. Du, G. Singh, C. J. H. Ho, S. Zhang, A. B. E. Attia, X. Li, and M. Olivo, "Fast pulsatile blood flow measurement in deep tissue through a multimode detection fiber," *J. Biomed. Opt.* **25**(5), 055003 (2020).
15. Z. Teng, F. Gao, H. Xia, W. Chen, and C. Li, "In vivo pulse wave measurement through a multimode fiber diffuse speckle analysis system," *Front. Phys.* **8**, 613342 (2021).
16. J. S. Richman and J. R. Moorman, "Physiological time-series analysis using approximate entropy and sample entropy," *Am. J. Physiol.-Heart Circ. Physiol.* **278**(6), H2039–H2049 (2000).
17. A. Delgado-Bonal and A. Marshak, "Approximate Entropy and Sample Entropy: A Comprehensive Tutorial," *Entropy* **21**(6), 541 (2019).
18. S. Kim, E. Kim, E. Anguluan, and J. G. Kim, "Sample entropy analysis of laser speckle fluctuations to suppress motion artifact on blood flow monitoring," *Chin. Opt. Lett.* **20**(1), 011702 (2022).
19. M. Aktaruzzaman and R. Sassi, "Parametric estimation of sample entropy in heart rate variability analysis," *Biomed. Signal Process. Control* **14**, 141–147 (2014).
20. X. Chen, I. Solomon, and K. Chon, "Comparison of the Use of Approximate Entropy and Sample Entropy: Applications to Neural Respiratory Signal," in *2005 IEEE Engineering in Medicine and Biology 27th Annual Conference* 4212–4215 (IEEE, 2005). doi:10.1109/IEMBS.2005.1615393
21. L. Montesinos, R. Castaldo, and L. Pecchia, "On the use of approximate entropy and sample entropy with centre of pressure time-series," *J. NeuroEngineering Rehabil.* **15**(1), 116 (2018).
22. J. R. Moorman, "A crossroads in predictive analytics monitoring for clinical medicine," *J. Electrocardiol.* **51**(6), S52–S55 (2018).
23. S. Simons, D. Abasolo, and J. Escudero, "Classification of Alzheimer's disease from quadratic sample entropy of electroencephalogram," *Healthc. Technol. Lett.* **2**(3), 70–73 (2015).
24. S. Qiao, M. Qin, and H. Wang, "Analysis of Knee Infrared Image Based on Sample Entropy Algorithm," in *2015 8th International Conference on Intelligent Networks and Intelligent Systems (ICINIS)* 1–4 (IEEE, 2015). doi:10.1109/ICINIS.2015.10
25. M. Ghijsen, T. B. Rice, B. Yang, S. M. White, and B. J. Tromberg, "Wearable speckle plethysmography (SPG) for characterizing microvascular flow and resistance," *Biomed. Opt. Express* **9**(8), 3937–3952 (2018).
26. A. Garrett, B. Kim, E. J. Sie, N. Z. Gurel, F. Marsili, D. A. Boas, and D. Roblyer, "Simultaneous photoplethysmography and blood flow measurements towards the estimation of blood pressure using speckle contrast optical spectroscopy," *Biomed. Opt. Express* **14**(4), 1594–1607 (2023).
27. S. Zilpelwar, E. J. Sie, D. Postnov, A. I. Chen, B. Zimmermann, F. Marsili, D. A. Boas, and X. Cheng, "Model of dynamic speckle evolution for evaluating laser speckle contrast measurements of tissue dynamics," *Biomed. Opt. Express* **13**(12), 6533–6549 (2022).
28. V. Dremine, I. Kozlov, M. Volkov, N. Margaryants, A. Potemkin, E. Zherebtsov, A. Dunaev, and I. Gurov, "Dynamic evaluation of blood flow microcirculation by combined use of the laser Doppler flowmetry and high-speed videocapillaroscopy methods," *J. Biophotonics* **12**(6), e201800317 (2019).
29. A. Stefanovska, M. Bracic, and H. D. Kvernmo, "Wavelet analysis of oscillations in the peripheral blood circulation measured by laser Doppler technique," *IEEE Trans. Biomed. Eng.* **46**(10), 1230–1239 (1999).
30. T. Durduran, R. Choe, W. B. Baker, and A. G. Yodh, "Diffuse optics for tissue monitoring and tomography," *Rep. Prog. Phys.* **73**(7), 076701 (2010).
31. M. S. Patterson, S. Andersson-Engels, B. C. Wilson, and E. K. Osei, "Absorption spectroscopy in tissue-simulating materials: a theoretical and experimental study of photon paths," *Appl. Opt.* **34**(1), 22 (1995).
32. H. Obrig, M. Neufang, R. Wenzel, M. Kohl, J. Steinbrink, K. Einhäupl, and A. Villringer, "Spontaneous low frequency oscillations of cerebral hemodynamics and metabolism in human adults," *NeuroImage* **12**(6), 623–639 (2000).
33. R. Cheng, Y. Shang, D. Hayes Jr, S. P. Saha, and G. Yu, "Noninvasive optical evaluation of spontaneous low frequency oscillations in cerebral hemodynamics," *NeuroImage* **62**(3), 1445–1454 (2012).
34. F. Ayers, A. Grant, D. Kuo, D. J. Cuccia, and A. J. Durkin, "Fabrication and characterization of silicone-based tissue phantoms with tunable optical properties in the visible and near infrared domain," in *Design and Performance*

Validation of Phantoms Used in Conjunction with Optical Measurements of Tissue (Vol. 6870, pp. 56–64). SPIE (2008).

35. A. P. Popov, A. V. Bykov, and I. V. Meglinski, “Influence of probe pressure on diffuse reflectance spectra of human skin measured in vivo,” *J. Biomed. Opt.* **22**(11), 110504 (2017).
36. I. Mizeva, I. Makovik, A. Dunaev, A. Krupatkin, and I. Meglinski, “Analysis of skin blood microflow oscillations in patients with rheumatic diseases,” *J. Biomed. Opt.* **22**(7), 070501 (2017).
37. E. Zhrebtsov, I. Kozlov, V. Dremin, A. Bykov, A. Dunaev, and I. Meglinski, “Diagnosis of skin vascular complications revealed by time-frequency analysis and laser Doppler spectrum decomposition,” *IEEE Trans. Biomed. Eng.* **70**(1), 3–14 (2023).
38. Student, “The Probable Error of a Mean,” *Biometrika* **6**(1), 1–25 (1908).